Influence of constitutive model in springback prediction using the split-ring test

Hervé Laurent, Renaud Grèze, Pierre-Yves Manach, Sandrine Thuillier

Influence of constitutive model in springback prediction using the split-ring test

H. Laurent [a,b,*], R. Grèze [a], P.Y. Manach [a], S. Thuillier [a]

[a] Université Européenne de Bretagne, Laboratoire d'Ingénierie des MATériaux de Bretagne (LIMATB - EG2M), Université de Bretagne-Sud, BP 92116, 56321 Lorient cedex, France
[b] CEMUC, Departamento de Engenharia Meca^nica, Universidade de Coimbra, Pinhal de Marrocos, 3030-201 Coimbra, Portugal

The aim of this paper is to compare several plastic yield criteria to show their relevance on the prediction of springback behavior for a AA5754-0 aluminum alloy. An experimental test similar to the Demeri Benchmark Test [Demeri MY, Lou M, Saran MJ. A benchmark test for springback simulation in sheet metal forming. In: Society of Automotive Engineers, Inc., vol. 01-2657, 2000] has been developed. This test consists in cutting a ring specimen from a full drawn cup, the ring being then split longitudinally along a radial plan. The difference between the ring diameters, before and after splitting, gives a direct measure of the springback phenomenon, and indirectly, of the amount of residual stresses in the cup. The whole deep drawing process of a semi-blank and numerical splitting of the ring are performed using the finite element code Abaqus. Several material models are analyzed, all considering isotropic and kinematic hardening combined with one of the following plasticity criteria: von Mises, Hill'48 and Barlat'91. This last yield criterion has been implemented in Abaqus. Main observed data are force–displacement curves during forming, cup thickness according to material orientations and ring gap after splitting. The stress distributions in the cup, at the end of the drawing stage, and in the ring, after springback, are analyzed and some explanations concerning their influence on springback mechanisms are given.

1. Introduction

Aluminum alloys are increasingly used in the automotive industry, with an average increase of 6% per year, due to environmental norms concerning the decrease of carbon dioxide releases. Thus, automotive industries, as well as tool makers, have to work with these types of material. As the mechanical design of parts and tools is almost entirely based on finite element simulation, there is a need for specific constitutive laws, specially concerning the initial anisotropy. Moreover, springback prediction presents a higher impact on tool design, since the yield stress over Young's modulus ratio is smaller than for steel.

In the field of metal forming at room temperature such as deep drawing or hemming, finite element simulation is nowadays widely used to design parts and tools with dedicated codes like PamStamp or Autoform. But, here there seems to be a gap between knowledge found in the scientific literature concerning the development of constitutive laws for aluminum alloys and day-to-day use in finite element codes. This gap comes essentially from the difficulty to identify material parameters with increasing complex models.

Springback prediction is also an urgent demand from tool makers, in order to avoid too many experimental trial steps before achieving the correct final shape of the part. It is now well established that modeling the behavior of metals during loading and reverse loading improves springback predictions. Kinematic hardening is then introduced in most industrial finite element codes, though its use is highly dependent on parameter identification (e.g. [2,3]).

For the numerical simulation of sheet metal forming processes, appropriate hardening model and plastic yield criterion that properly describe material behavior at large strain is needed. An accurate description of the mechanical behavior is very important, especially for springback analysis. Over the years, a lot of yield functions have been introduced to describe the initial plastic anisotropy of sheet metals, e.g. a review of the anisotropic yield criteria can be found in [4]. The main difficulty is to take into account both the different stress levels at different orientations to the RD (rolling direction) and also the anisotropy coefficients r_α. The most commonly used yield criterion is still Hill's anisotropic quadratic yield function (Hill'48). But, the Hill'48 criterion is often

* Corresponding author at: Université Européenne de Bretagne, Laboratoire d'Ingénierie des MATériaux de Bretagne (LIMATB - EG2M), Université de Bretagne-Sud, BP 92116, 56321 Lorient cedex, France.
E-mail address: herve.laurent@univ-ubs.fr (H. Laurent).

criticized for its application to metals with low r-values such as aluminum alloys (e.g. [5–9]). Another widely used yield function is the Barlat'91 yield criterion [10], which is a six-component yield function involving a linear transformation of the stress state (recently extended in [9,11]). In general, with this yield criterion, there was a satisfactory correlation with the experimental data (e.g. [7,12,13]).

In the recent years, several experimental tests have been developed for springback characterization, like draw-bend and flanging tests [14]. However, while those tests are preferred in understanding certain aspects of springback, they are not truly deep drawing operations as is usually seen in industrial stamping operations. In the last few years, one test has received an increasing amount of attention: the split-ring test, following Demeri test procedure [1]. This test provides a simple effective benchmark for correlative forming and springback predictive capabilities with experimental measures [14–20]. The experimental procedure consists in the deep drawing of a cylindrical cup, the cutting of a ring in the mid-section of the cup and then a splitting of the ring to let it open up. The splitting operation relieves the internal stresses and creates a large springback; therefore, the ring opening can reach high values, which reduces the experimental gap. Residual stresses in the cup exist because different locations in the cup have accumulated different magnitudes of plastic strain during draw-bend-unbend process. The through-thickness residual stresses predicted at the end of the forming process are responsible for the bending momentum that changes the shape of the split ring.

The aim of this paper is to investigate the capability of different yield criteria, with both isotropic and mixed hardening, to represent the behavior of an aluminum alloy during a forming process and springback evolution using the split-ring test. To test the accuracy of these constitutive models, finite element simulations were carried out using Abaqus [21] and compared with well-established experimental results. All simulations were performed with a fixed set of numerical parameters in order to mainly investigate the influence of the constitutive model on springback prediction.

2. Constitutive equations

To achieve objectivity in large deformation continuum mechanics, the co-rotational moving frame [22–24] has been chosen to formulate the constitutive equations. This local objective frame is defined such as the local spin tensor is equal to zero which leads to the definition of the rotation matrix $\boldsymbol{Q}$ from the sample frame to the co-rotational frame:

$$\dot{\boldsymbol{Q}} = -\boldsymbol{Q}\boldsymbol{\Omega} \quad \text{and} \quad \boldsymbol{Q}_{(t=0)} = \boldsymbol{0} \tag{1}$$

with $\boldsymbol{\Omega}$ the spin tensor.

Stress and strain tensors are expressed in this co-rotational frame and the splitting of the deformation in elastic $\boldsymbol{\varepsilon}^e$ and (visco)plastic $\boldsymbol{\varepsilon}^{vp}$ parts is assumed:

$$\boldsymbol{\varepsilon} = \boldsymbol{\varepsilon}^e + \boldsymbol{\varepsilon}^{vp} \tag{2}$$

Rates are defined by the Jaumann derivative, which correspond to the derivative in the co-rotational frame.

Elasticity is assumed isotropic:

$$\boldsymbol{\sigma} = \boldsymbol{C}^e : \boldsymbol{\varepsilon}^e \tag{3}$$

where $\boldsymbol{\sigma}$ defines the co-rotated Cauchy stress tensor, $\boldsymbol{C}^e$ the elastic modulus tensor, which depends on Lamé's coefficients λ and μ.

2.1. Yield criterion description

In the following, vectors $\vec{1}$, $\vec{2}$ and $\vec{3}$ are co-linear, respectively, to the tensile direction (RD), the transverse direction (TD) and the normal direction (ND) to the sheet plane.

The yield surface is defined by $\phi(\boldsymbol{\sigma}, R, \boldsymbol{X}) = 0$ which depends on the Cauchy stress tensor $\boldsymbol{\sigma}$, a scalar internal variable R which represents isotropic hardening and a tensorial internal variable $\boldsymbol{X}$ for the kinematic hardening. Introducing the equivalent stress $\bar{\sigma}$, this yield surface can also be defined by

$$\phi(\boldsymbol{\sigma}, R, \boldsymbol{X}) = \bar{\sigma}(\boldsymbol{\sigma}, \boldsymbol{X}) - R = 0 \tag{4}$$

Elasticity is defined within the condition $\phi < 0$, and there is:

- yield, when $\phi = 0$ and $\partial\phi/\partial\boldsymbol{\sigma} : \dot{\boldsymbol{\sigma}} > 0$
- or elastic unloading, if $\phi = 0$ and $\partial\phi/\partial\boldsymbol{\sigma} : \dot{\boldsymbol{\sigma}} \leqslant 0$.

Within the general framework of non-associated plasticity, the generalized normality rule gives the strain rate tensor $\boldsymbol{D}^p$:

$$\boldsymbol{D}^p = \dot{\chi}\frac{\partial\phi}{\partial\boldsymbol{\sigma}} \quad \text{or} \quad \boldsymbol{D}^p = \dot{\chi}\frac{\partial\phi}{\partial\boldsymbol{\sigma}'} \tag{5}$$

where $\dot{\chi}$ is a scalar and $\boldsymbol{\sigma}'$ the deviatoric stress tensor.

In this study, different yield criteria and hardening laws are tested in order to check their influence on the prediction of deep drawing and springback:

(1) von Mises yield criterion with isotropic strain hardening referred to as *vonMises*,
(2) von Mises yield criterion with combined isotropic hardening, kinematic hardening and viscous part, referred to as $vonMises + KH$,
(3) Hill'48 yield function with isotropic hardening or with combined isotropic and kinematic hardening and viscous part, referred to as $Hill48 - evp$ and $Hill48 - evp + KH$, respectively,
(4) and finally, Barlat'91 yield criterion with isotropic hardening or with combined isotropic and kinematic hardening and viscous part, referred to as $Barlat91$ and $Barlat91 + KH$, respectively.

The *vonMises* yield function is directly used in Abaqus standard code with an elastoplastic approach. The $vonMises + KH$, $Hill48 - evp$ and $Barlat91$ (with or without kinematic hardening (KH)) models are implemented via a user's material [25] Abaqus subroutine (*Umat*) within an elasto-viscoplastic framework. These models are detailed in the next paragraph.

2.1.1. Hill'48 yield function

The quadratic yield function proposed by Hill [26] is a widely used anisotropic yield function. It is also known as Hill'48 to distinguish it from later models. In this yield function three orthogonal planes of symmetry are presumed, leading to three principal axes of anisotropy. Using the effective stress tensor $\boldsymbol{\sigma}^X = \boldsymbol{\sigma} - \boldsymbol{X}$, the Hill yield function can be written as

$$\begin{aligned}\phi = {} & H(\sigma^X_{11} - \sigma^X_{22})^2 + G(\sigma^X_{11} - \sigma^X_{33})^2 + F(\sigma^X_{33} - \sigma^X_{22})^2 + 2N{\sigma^X_{12}}^2 \\ & + 2M{\sigma^X_{13}}^2 + 2L{\sigma^X_{23}}^2 = \bar{\sigma}^2\end{aligned} \tag{6}$$

with the subscripts 1, 2 and 3 referring to the principal axes of orthotropy.

F, G, H, L, M and N are the six material parameters that depend on the flow stress under uniaxial and shear loading in the principal directions, respectively. This criterion implicitly assumes that hydrostatic stress states do not lead to plastic yielding.

2.1.2. Barlat'91 yield criterion

The Barlat'91 yield criterion [10] is derived from the one proposed by Hershey [27] and Hosford [28]. This criterion was developed for anisotropic materials and gives a good representation of yield surfaces calculated with polycrystalline models when the parameter $m_b = 6$ and 8 for *BCC* and *FCC* materials, respectively. It is also interesting to note that this function reduces to the von Mises criterion for $m_b = 2$ and 4 and to the Tresca criterion for $m_b = 1$ and ∞. The Barlat'91 yield function ϕ is given by

$$\phi = |S_1 - S_2|^{m_b} + |S_2 - S_3|^{m_b} + |S_3 - S_1|^{m_b} = 2\bar{\sigma}^{m_b} \tag{7}$$

where $S_{i=1,2,3}$ are the eigenvalues of the deviatoric tensor $\boldsymbol{S}$ obtained by a linear transformation of the effective stress tensor:

$$\begin{aligned}
S_{11} &= \tfrac{1}{3}\left[c_b(\sigma^X_{11} - \sigma^X_{22}) - b_b(\sigma^X_{33} - \sigma^X_{11})\right] \\
S_{22} &= \tfrac{1}{3}\left[a_b(\sigma^X_{22} - \sigma^X_{33}) - c_b(\sigma^X_{11} - \sigma^X_{22})\right] \\
S_{33} &= \tfrac{1}{3}\left[b_b(\sigma^X_{33} - \sigma^X_{11}) - a_b(\sigma^X_{22} - \sigma^X_{33})\right] \\
S_{23} &= f_b\sigma^X_{23} \\
S_{31} &= g_b\sigma^X_{31} \\
S_{12} &= h_b\sigma^X_{12}
\end{aligned} \tag{8}$$

a_b, b_b, c_b, f_b, g_b, h_b, m_b are the material parameters which define the shape of the yield surface. Following the work of [29], the eigenvalues of $\boldsymbol{S}$ are expressed with complex numbers, depending on the coefficients of the characteristic equation of $\boldsymbol{S}$:

$$\lambda^3 - 3I_2\lambda - 2I_3 = 0 \tag{9}$$

where $-3I_2$ and $2I_3$ are the second and third principal invariants of $\boldsymbol{S}$, respectively.

Calculation of the viscoplastic strain increment requires the knowledge of the gradient of ϕ with respect to the stress tensor (5). Calculations of these components are given in [29] and will not be detailed here.

The choice has been made to impose that the initial equivalent stress is equal to the initial elastic limit in RD, whatever the anisotropy coefficients. Writing such a condition in the case of a uniaxial stress state leads to another equation between coefficients b_b and c_b such as

$$\frac{1}{2}\left[\frac{1}{3^{m_b}}(|2c_b + b_b|^{m_b} + |b_b - c_b|^{m_b} + |-2b_b - c_b|^{m_b})\right] - 1 = 0 \tag{10}$$

For a given b_b value, c_b is calculated from this non-linear equation, solved by using a Newton–Raphson algorithm.

2.1.3. Elasto-viscoplastic behavior

For simplicity's sake, a viscoplastic potential is used to determine directly the viscoplastic multiplier $\dot{\lambda}$:

$$\dot{\lambda} = \left(\frac{\bar{\sigma} - R}{K}\right)^N \tag{11}$$

where N, K are material parameters.

In the case of an isotropic evolution of the yield surface, a Hocket–Sherby form law has been chosen to describe the work hardening:

$$R = \sigma_{sat} - (\sigma_{sat} - \sigma_0)\exp(-C_R(\bar{\varepsilon}^{vp})^n) \tag{12}$$

where $\bar{\varepsilon}^{vp}$ is the equivalent viscoplastic strain, σ_0 is the initial elastic limit in RD, $(\sigma_{sat} - \sigma_0)$ is the isotropic hardening range and C_R the saturation rate. It should be noted that Eq. (12) leads to a Voce type evolution when $n = 1$.

The evolution of the back-stress tensor $\boldsymbol{X}$ is described with the Armstrong–Frederick law [30] and with a Prager type contribution, to fully capture both the rapid evolution of the back-stress just after reloading and its evolution for larger strains:

$$\boldsymbol{X} = \tfrac{2}{3}(C_X\,\boldsymbol{\alpha} + H_X\,\boldsymbol{\varepsilon}^{vp}) \tag{13}$$

with

$$\dot{\boldsymbol{\alpha}} = \dot{\boldsymbol{\varepsilon}}^{vp} - B_X\dot{\bar{\varepsilon}}^{vp}\boldsymbol{\alpha} \tag{14}$$

where C_X/B_X determines the intensity of the non-linear kinematic work hardening and H_X is the slope of the linear part of the kinematic hardening.

The internal variable $\boldsymbol{\alpha}$ is associated to $\boldsymbol{X}$ and $\bar{\varepsilon}^{vp}$ is the cumulated viscoplastic strain defined by

$$\bar{\varepsilon}^{vp} = \int_0^t \sqrt{\frac{2}{3}\boldsymbol{D}^p : \boldsymbol{D}^p}\,\mathrm{d}t \tag{15}$$

3. Material and mechanical characterizations

The studied material is a 5000 series Al–Mg alloy, AA5754-0. It is often used in the automotive industry for inner body panels. Cold-rolled sheets are 1 mm thick. Their typical composition is given in Table 1.

To test the sheet samples under different stress and strain paths, mechanical testings are performed through uniaxial tensile tests and monotonic and cyclic shear tests (i.e. Bauschinger shear tests). Local strains are measured using either a longitudinal extensometer in the case of uniaxial tension or a high resolution video camera [31]. In this case, three dots are drawn over the sample surface; the 2D strain tensor is derived from the evolution of the scalar product of two vectors built from these dots. Therefore, all components of the planar strain tensor are recorded during the test. The resolution is 5×10^{-3}, to be compared to the resolution of the extensometer of 5×10^{-5}. Though the resolution of the optical device is lower, it gives additional information such as transverse strain in uniaxial tension and a local strain measurement in shear. Five tests are performed to check the reproducibility of the results and one is chosen as representative of the behavior.

Table 1
Composition in weight % of aluminum AA5754-0.

Cu	Mn	Mg	Si	Fe	Cr	Al
$\leqslant$0.10	$\leqslant$0.500	2.60–3.60	$\leqslant$0.400	$\leqslant$0.400	$\leqslant$0.300	93.6–97.3

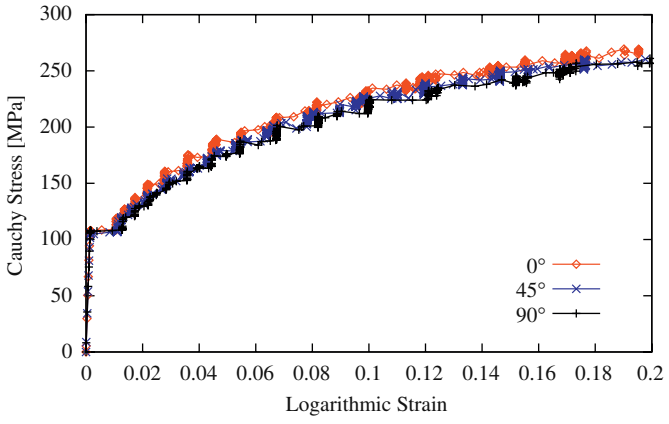

Fig. 1. Uniaxial tensile test at 0°, 45° and 90° to RD.

3.1. Tensile tests

Rectangular samples of $20 \times 180 \times 1\,\text{mm}^3$ are cut at several orientations to RD (0°, 45° and 90°). The samples are then machined along the longitudinal dimension to remove the hardened zone. Logarithmic strain and Cauchy stress are used to plot stress–strain data. The strain rate is of $\dot{\varepsilon} = 10^{-3}\,\text{s}^{-1}$. The results obtained in the three orientations to RD are very similar (Fig. 1).

The discontinuous effect, observed in Fig. 1, is related to a dynamic ageing of the alloy, due to interaction between mobile dislocations and magnesium atoms in solid solution in a given temperature/strain rate range [32]. Plasticity is localized in bands which propagate during straining (Portevin–Le Châtelier effect).

As can be observed in Fig. 1, this material exhibits rather similar stress levels whatever the orientation to RD. Plastic strain ratios $r_\alpha = \text{d}\varepsilon^p_{yy}/\text{d}\varepsilon^p_{zz}$ are calculated from the volume conservation in the plastic domain and are plotted in Fig. 2. In this case, $\vec{x}$ corresponds to the tensile direction, $\vec{y}$ the in-plane perpendicular direction of the plane and $\vec{z}$ the through-thickness direction.

Table 2 gives the mechanical properties determined from tensile tests. Young's modulus is slightly dependent on the orientation, its average value is 74 430 MPa and Poisson's ratio is fixed at 0.33, which is a typical value for FCC materials. The mean anisotropy coefficient, which characterizes the normal anisotropy, is given by $r_{medium} = (r_0 + r_{90} + 2\,r_{45})/4 = 0.68$. This value is significant and therefore the normal anisotropy is important. The planar anisotropy, characterized by $\Delta r = (r_0 + r_{90} - 2\,r_{45})/2 = 0.14$ is also significant.

Another cross-view through the experimental results is given in Fig. 3. Here, on a uniaxial tensile test, for a specimen at 90° to RD, the influence of the strain rate is investigated. First, a strain rate of $\dot{\varepsilon} = 10^{-4}\,\text{s}^{-1}$ is used up to a strain of 0.04, followed by a relaxation during 240 s, then a strain rate of $\dot{\varepsilon} = 10^{-3}\,\text{s}^{-1}$ up to 0.08, followed also by a relaxation during 240 s, thirdly a strain rate of $\dot{\varepsilon} = 10^{-2}\,\text{s}^{-1}$ up to 0.12, and finally a strain rate of $\dot{\varepsilon} = 10^{-3}\,\text{s}^{-1}$. At room temperature, it can be seen that the material behavior is not affected by the strain rate changes.

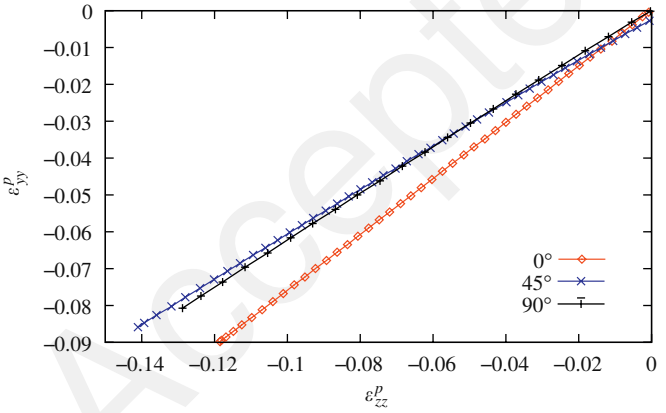

Fig. 2. Calculation of Hill plastic strain ratios by measuring the slope in the $\varepsilon^p_{yy} = f(\varepsilon^p_{zz})$ diagram.

Table 2
Yield stress and Hill plastic strain ratios at several orientations to RD.

Orientation/RD	0°	45°	90°
E (MPa)	74 620	75 050	73 620
$Rp_{0.2}$ (MPa)	107.6	105.5	107.0
r_α	0.82	0.61	0.68

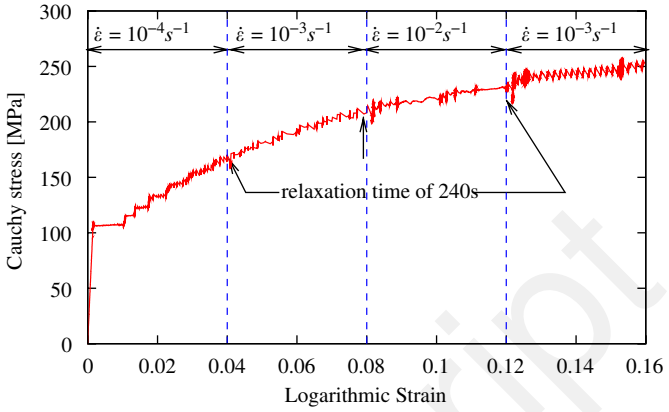

Fig. 3. Strain rate influence on uniaxial tensile test at 90° to RD.

3.2. Shear tests

A shear device developed for metallic sheets is used [31,33]. Samples are rectangular and the dimensions of the gauge area are $4.5 \times 50 \times 1$ mm (Fig. 4). In the case of thin sheets and for a gauge length over width ratio higher than 10, the strain is rather homogeneous in the central zone [34]. The local strain tensor is measured in the middle of the sample and the shear strain γ is calculated from the components of the strain tensor. Strain reversal is achieved by moving the mobile grip in the opposite direction. The strain rate is fixed to $\dot{\gamma} = 2 \times 10^{-3}\,\text{s}^{-1}$. Monotonic uniaxial shear tests are carried out at several orientations to RD: 0°, 45° and 90° (Fig. 5) whereas Bauschinger shear tests are performed only in RD (Fig. 6).

4. Identification of material parameters

Inverse parameter identification is performed with the dedicated tool SiDoLo [35,36]. The experimental database is composed of tensile tests at 0°, 45° and 90° to RD including both stress–strain curves and evolution of the plastic transverse strain vs the plastic width strain. It also includes shear tests at three different orientations to RD including monotonic tests as well as Bauschinger test after a shear pre-strain of 0.1, 0.2 and 0.3 in RD. Therefore, the database consists of tests with two observable variables, namely stress and strain components. A different weighting coefficient is affected for each of these observable variables, the value of which is chosen according to the uncertainty on the experimental measures. For the shear stress, the value of the weighting coefficient is $\Delta\sigma_{xy} = 3$ MPa and for the tensile tests, $\Delta\sigma_{xx} = 5$ MPa and $\Delta\varepsilon_{xx} = 0.005$ [8,36,37].

During identification, Young's modulus and Poisson's ratio are fixed to $E = 74\,620$ MPa and $\nu = 0.33$, respectively. Fig. 3 shows the weak influence of the strain rate so that the viscous parameters are fixed to $K = 4\,\text{MPa}\,\text{s}^{1/N}$ and $N = 5$, which leads to a viscous contribution lower than 1 MPa. For all yield criteria, the initial equivalent stress is equal to the initial elastic limit in the RD, whatever the anisotropy coefficients. Thus, for the *Hill*48 − *evp* yield criterion, parameters G and H verify $G + H = 1$; parameters L and M are also fixed at 1.5. For the *Barlat*91 yield criterion, the relationship between b_b and c_b given by Eq. (10) is imposed; parameters $f_b = g_b = 1$ and $m_b = 8$ are fixed.

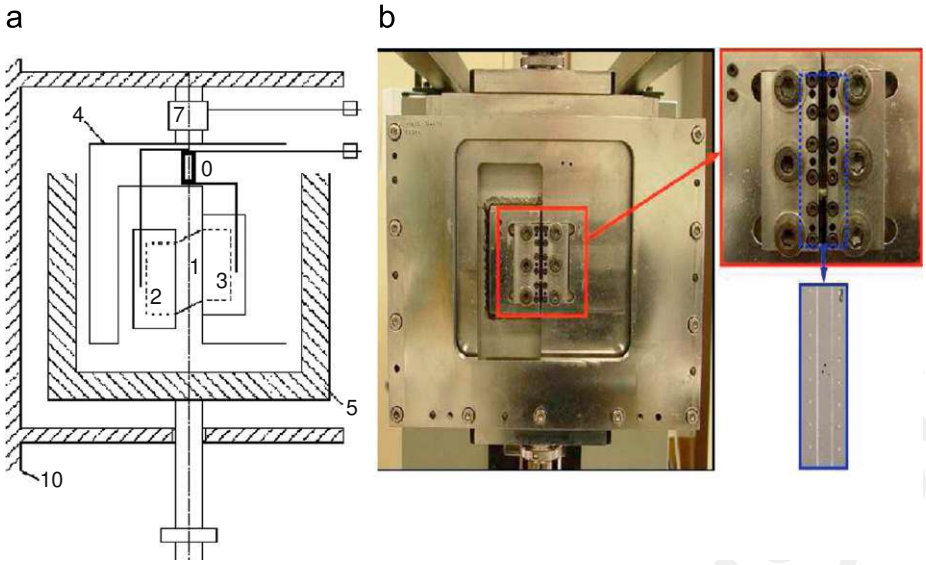

Fig. 4. Experimental device for the shear test: (a) schematic view of the device, (b) grips system (in red) with specimen (in blue). (For interpretation of the references to color in this figure legend, the reader is referred to the web version of this article.)

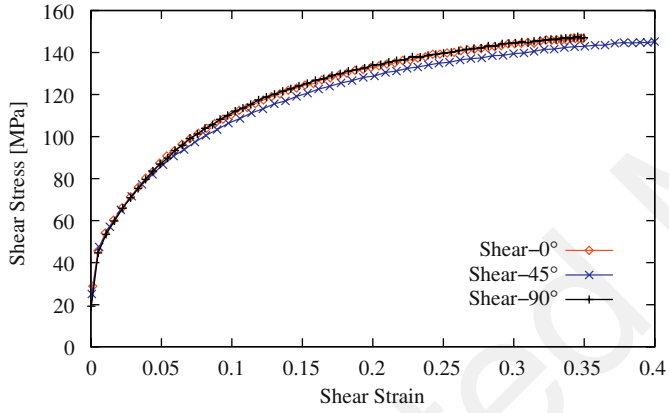

Fig. 5. Monotonic shear test results at 0°, 45° and 90° to RD.

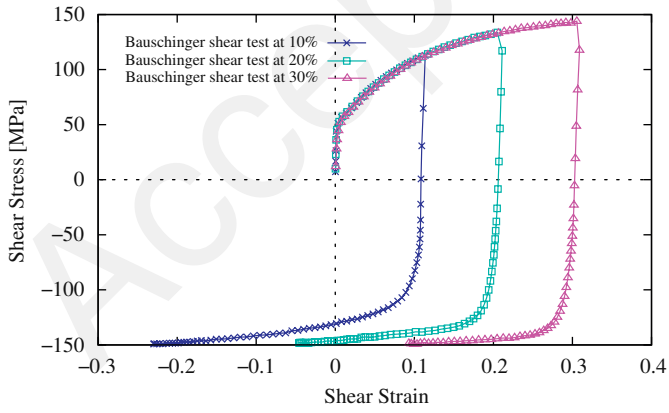

Fig. 6. Bauschinger shear test results in RD.

Material parameters are given in Tables 3–5 for the different yield criteria. The label "+KH" is added if the kinematic hardening is also taken into account in the constitutive modeling. Identified curves show good agreement on anisotropy for tensile and shear test simulations. The identification results for all criteria are very similar and only the results for the *Barlat*91 criterion with or without kinematic hardening (Figs. 7 and 8, respectively) are presented. These figures show that the material exhibits only a weak kinematic contribution to the hardening. Taking into account this contribution mainly influences the behavior upon reloading. Whatever the yield criterion, the kinematic contribution, described with a saturation Voce type equation and a linear term, evolves very rapidly with equivalent plastic strain to the saturation value. This rapid evolution at the onset of plastic yielding influences significantly the initial yield stress.

Table 3
Material parameters corresponding to *vonMises* and *vonMises* + *KH* yield criteria and error function value at the end of the inverse analysis procedure.

Isotropic hardening	Mixed hardening	
$\sigma_0 = 87.3$ MPa	$\sigma_0 = 51.3$ MPa	$C_X = 9997.5$ MPa
$\sigma_{sat} = 264.6$ MPa	$\sigma_{sat} = 197.3$ MPa	$B_X = 150.4$
$C_R = 14.9$	$C_R = 11.23$	$H_X = 99.9$ MPa
$n = 0.980$	$n = 1$	
error $= 533.8$	*error* $= 280.9$	

Table 4
Material parameters corresponding to *Hill*48 − *evp* and *Hill*48 − *evp* + *KH* yield criteria and error function value at the end of the inverse analysis procedure.

Isotropic hardening	Mixed hardening	
$\sigma_0 = 88.6$ MPa	$\sigma_0 = 55.3$ MPa	$C_X = 9692.8$ MPa
$\sigma_{sat} = 269.3$ MPa	$\sigma_{sat} = 208.7$ MPa	$B_X = 156.0$
$C_R = 14.9$	$C_R = 11.3$	$H_X = 99.4$ MPa
$n = 0.969$	$n = 1$	
Hill'48 parameters		
$F = 0.6979$	$F = 0.9660$	
$G = 0.5511$	$G = 0.5943$	
$H = 0.4489$	$H = 0.4057$	
$N = 1.5445$	$N = 1.6701$	
error $= 412.2$	*error* $= 146.2$	

Table 5
Material parameters corresponding to *Barlat91* and *Barlat*91 + *KH* yield criteria and error function value at the end of the inverse analysis procedure.

Isotropic hardening	Mixed hardening	
$\sigma_0 = 91.7$ MPa	$\sigma_0 = 55.4$ MPa	$C_X = 9348.2$ MPa
$\sigma_{sat} = 276.7$ MPa	$\sigma_{sat} = 209.9$ MPa	$B_X = 141.6$
$C_R = 14.3$	$C_R = 10.9$	$H_X = 86.6$ MPa
$n = 0.983$	$n = 0.999$	
Barlat'91 parameters		
$a_b = 1.1136$	$a_b = 1.2853$	
$b_b = 1.0362$	$b_b = 1.1002$	
$c_b = 0.9627$	$c_b = 0.8913$	
$h_b = 0.9961$	$h_b = 0.9977$	
$error = 367.4$	$error = 132.5$	

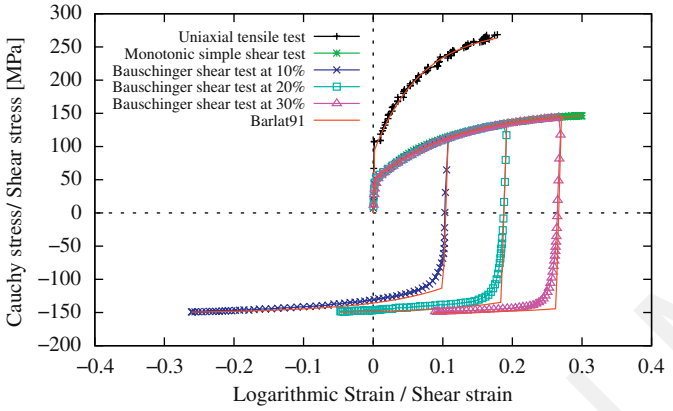

Fig. 7. Comparison between experimental and identification for the tensile test, monotonic and Bauschinger simple shear tests in RD without kinematic hardening and *Barlat*91 criteria.

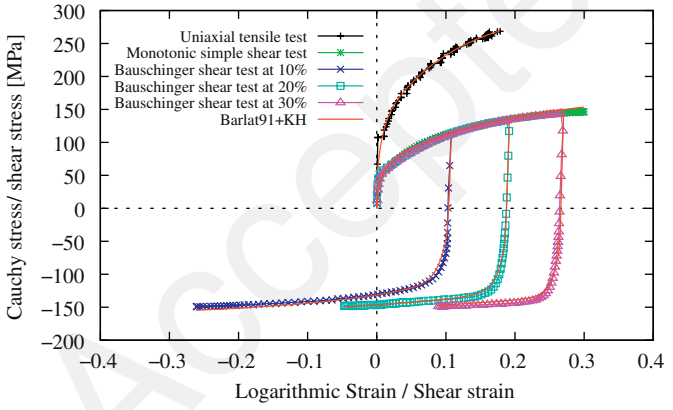

Fig. 8. Comparison between experimental and identification for the tensile test, monotonic and Bauschinger simple shear tests in RD with kinematic hardening and *Barlat*91 criteria.

Projections of the yield surfaces in the plane $\sigma_{yy} - \sigma_{xx}$ are plotted in Fig. 9 by using quantities normalized by the initial yield stress in RD. The yield stress under balanced biaxial stress conditions was not determined experimentally, leading to the shape of the yield surface uncertain in this region of the stress space. The parameter identification results could be improved by means of experimental data concerning this equibiaxial stress state [37–41].

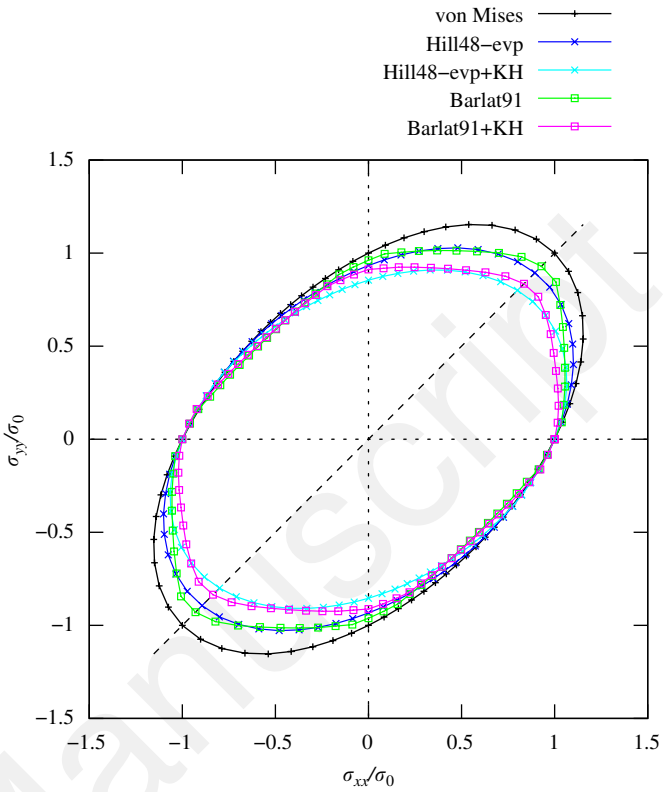

Fig. 9. Projections of the yield surface in the plane $(\sigma_{yy}/\sigma_0,\ \sigma_{xx}/\sigma_0)$ for all constitutive models used.

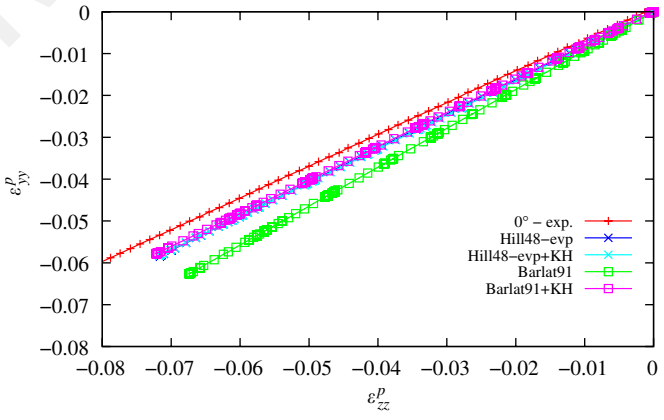

Fig. 10. Influence of yield criteria on the description of anisotropy coefficient in RD.

The identification procedure is based on the minimization of a error function with a gradient type algorithm. This function is defined in the least square sense. The error function value at the end of the inverse analysis procedure is also presented in Tables 3–5. These values are function of initial parameters and give an information on the best yield criteria parameters for a given hardening law (i.e. isotropic hardening or kinematic hardening). Taking into account the kinematic hardening reduces these errors. These results also show that the *Barlat*91 criterion with or without kinematic hardening leads to the lowest values of the error function.

A comparison between different yield criteria when taking anisotropy coefficient into account is presented in Figs. 10 and 11, for r_0 and r_{90}, respectively. As whole, there is a good description of the experimental results. The material behavior presents a weak

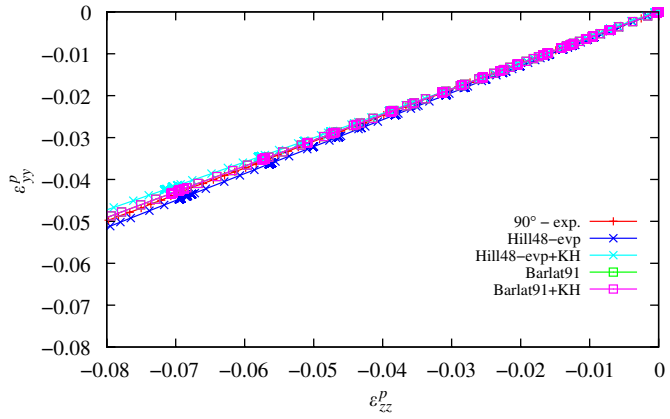

Fig. 11. Influence of yield criteria on the description of anisotropy coefficient at 90° to RD.

dependence on the orientations to RD for the stress level but a significant one regarding the *r*-ratios values. For this reason, the modeling of the stress–strain curves in tensile and shear tests can be well predicted by the *von Mises* criterion, but the modeling of strain effects (such as thickness variation) needs the use of a more complex criterion.

5. Experimental procedure

5.1. Deep drawing test

An experimental device has been used to draw cylinder cups; the dimensions of the tools and the blank are defined in Fig. 12 [6]. A blankholder adjusted on the punch diameter and allowing for force control has been developed for this study. The blankholder force is maintained by eight screws with Belleville washers stacked both parallel and in series. Force washers are also used to control the blankholder pressure during all the drawing stages.

Experiments are carried out at room temperature on a tensile test machine *Instron* 8803 of 500 kN maximum load capacity. The blankholder force imposed is 24 kN and the drawing speed is 0.5 mm s^{-1}. Blanks are lubricated on both sides at the beginning of the process (Yushrio Former FD-1500) and cups are drawn down to a punch displacement of 60 mm. At the end of forming, outer diameter of the cups is 104.5 mm and the height is around 46 mm. Experimental curves are representative of the average values of three tests. The experimental force–displacement curves of the punch are presented in Fig. 13. Maximum force obtained during forming is near 54 kN with a maximum error of 7%.

The thickness distributions in the cup wall, measured using a 3D measuring machine at 0°, 45° and 90° to RD, are presented in Fig. 14. The presented results are selected among all experimental results to be representative of the thickness distribution. All directions present a thinning in the cup's bottom, which comes from the stretching of the sheet at the beginning of the drawing. Conversely, thickening occurs in the cup's top due to a circumferential compression stress state under the blankholder. The thickness distributions at 45° and 90° are similar, but different from the one in RD. The cups were measured at a number of points along their height giving the wall inner and outer profiles (Fig. 15). This shape is due to the gap between the die and the punch which produces a stretching and curvature of the blank.

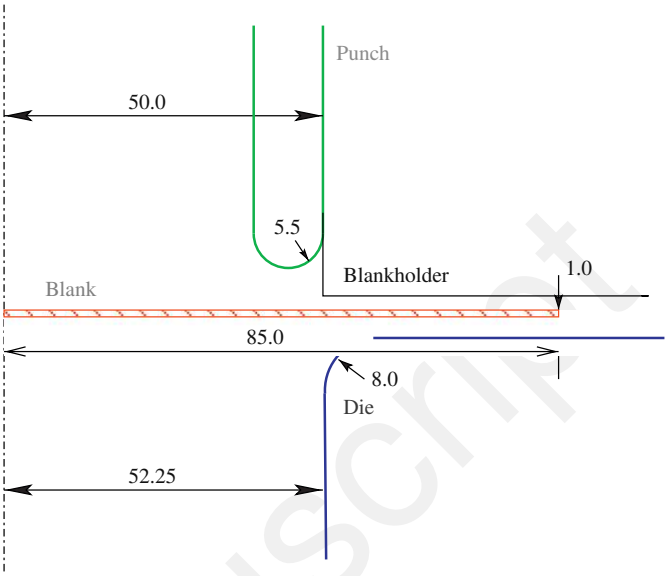

Fig. 12. Tool geometries (in mm) of the experimental device.

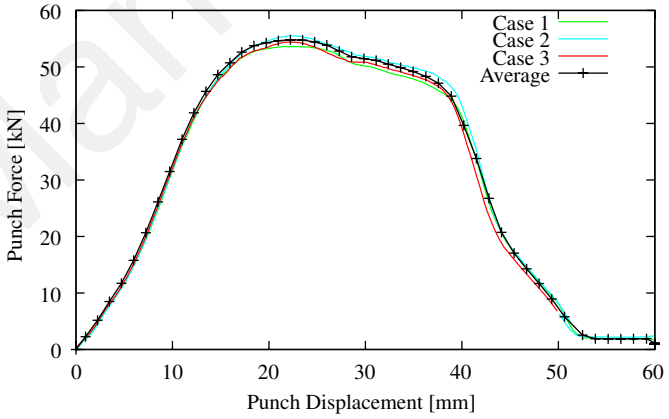

Fig. 13. Three experimental force–displacement curves of the punch and average experiment retained.

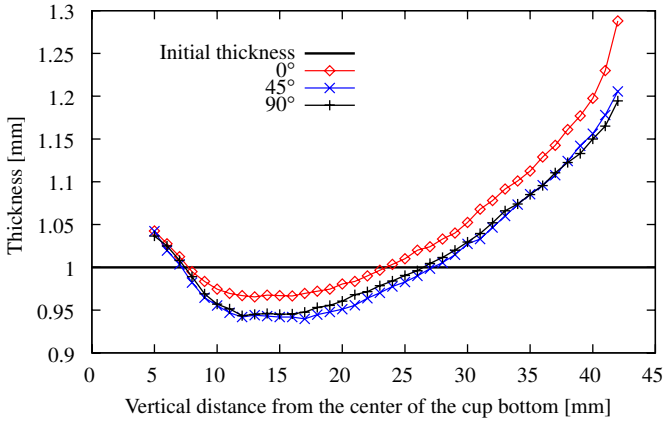

Fig. 14. Experimental thickness distribution in the cup wall at 0°, 45° and 90° to the RD.

5.2. Split-ring test

Rings from the formed cups are cut by machining at 15 mm from the cup bottom. The rings are 20 mm high and have an ideal internal

diameter of 100 mm before splitting (Fig. 16). The rings are then split along the axial direction in RD to allow for opening up and springback, as shown in Fig. 17. The amount of change in the ring's diameter is a measure of the residual stresses released and, consequently, of springback. Experimental springback data consist of ring gap G measured along straight lines connecting the two ends of the split rings using a 3D measuring machine. The experimental value of $G = 64$ mm is average value obtained after six tests (the lowest value is 60 mm and the greatest 64.5 mm). It has to be noticed that due to the non-homogeneity of through-thickness stress distribution, the rings are no longer cylindrical after springback.

6. Numerical results

To test the influence of the constitutive models, simulations of the forming, ring trimming and springback after splitting are performed using Abaqus and compared with the above-presented experimental results. The *Hill*48 – *evp*, *Barlat*91 yield criteria, with or without kinematic hardening, are implemented via the *User Interface Material Umat*, whereas *Abaqus Standard* is used for the *vonMises* criterion.

The geometry of the blank and the tools is axisymmetric. However, due to the operation of ring cutting, an axisymmetric 2D analysis cannot be performed. A 3D analysis, with 8-node finite elements with linear interpolation, modeling only the deep drawing of a half blank is achieved. The chosen element is the C3D8I in which incompatible deformation modes are added as internal to the degrees of freedom in displacement [21]. This element is in the field of enhanced assumed strain formulation which showed its advantages in several applications (i.e. [42–44]). In all simulations of this paper, the FE mesh is identical and composed of 6510 elements with three layers in the thickness and 2170 elements in the sheet plane (Fig. 18). The type and the number of elements and nodes were first optimized in a parametric study.

The blank is subdivided into three parts at the beginning of the numerical simulation to allow for ring cutting. A symmetry boundary condition is defined along the global X-axis; the global Z-axis is parallel to the punch displacement direction. Analytical rigid tools are used. The blankholder force is kept constant at 12 kN during the drawing stage and the blank is drawn down to 60 mm. The friction coefficient used is 0.18.

At the end of deep drawing a first springback is predicted due to the removal of the drawing tools, by tools displacement. After this operation, ring cutting is performed by removing useless parts using the $*$*Model change* option in Abaqus [21]. This option removes parts of the mesh which do not form the ring. Just prior to the removal step, Abaqus stores the forces/fluxes that the

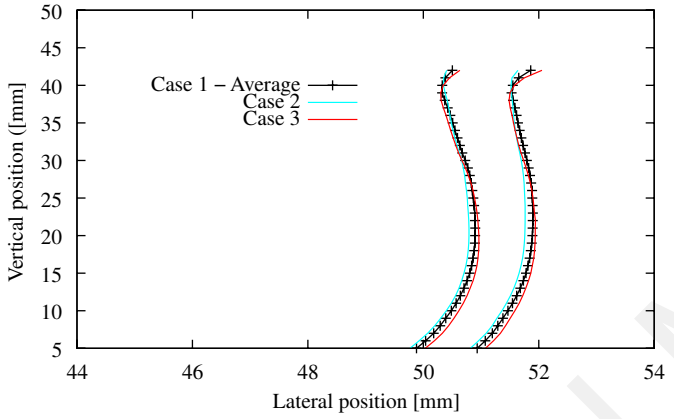

Fig. 15. Evolution of the wall profile, for the inner and outer surfaces in RD and average experiment retained.

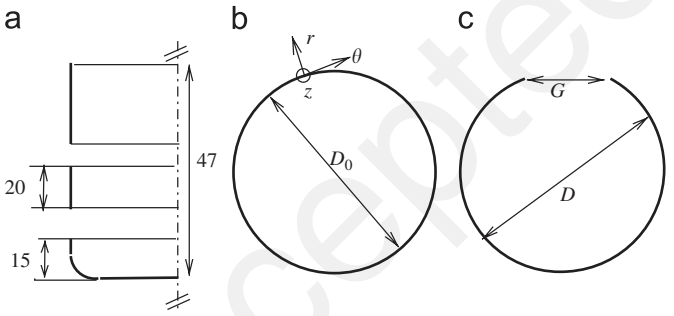

Fig. 16. Schematic representation of the ring cut from the deep-drawn cup. (a) Position of the cut in the wall (b) the ring before splitting with an ideal internal diameter of $D_0 = 100$ mm and (c) the ring after splitting and springback. G is the measured gap produced in the split ring due to springback.

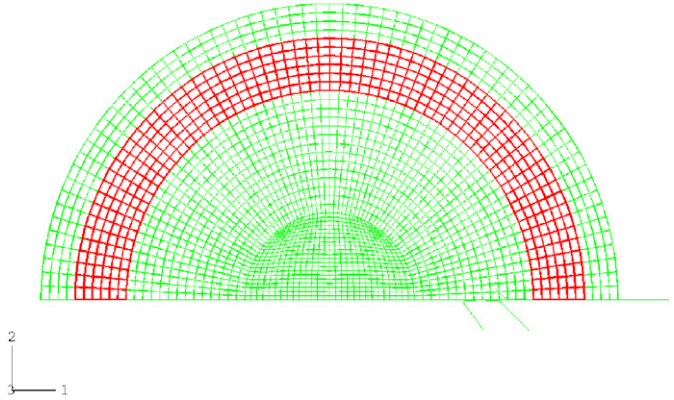

Fig. 18. Mesh used during the simulation and region in red corresponding to the ring. (For interpretation of the references to color in this figure legend, the reader is referred to the web version of this article.)

Fig. 17. From left to right, experimental drawn cup, cut rings and springback after splitting.

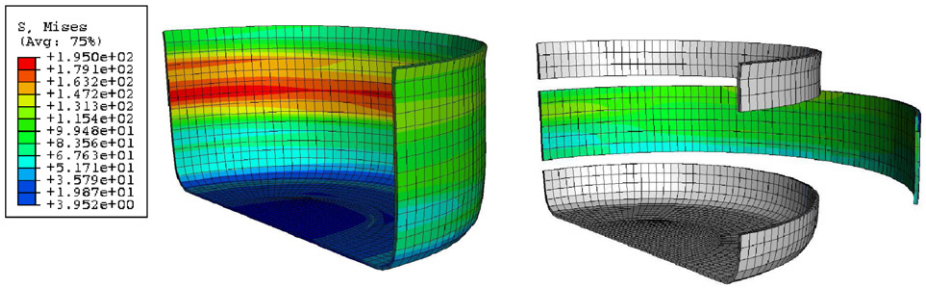

Fig. 19. Example of numerical drawn cup and springback after splitting in using *Barlat*91 criterion.

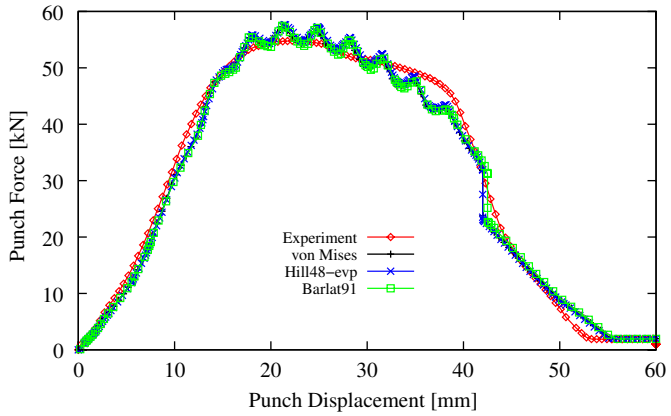

Fig. 20. Comparison between experimental and numerical results for the evolution of force during forming process for *vonMises*, *Hill*48 – *evp* and *Barlat*91 criteria without kinematic hardening.

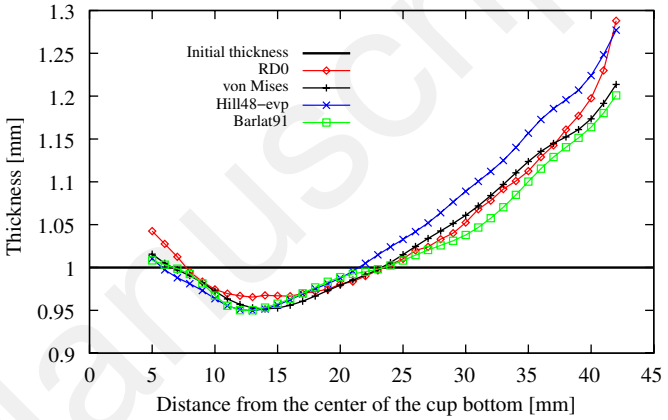

Fig. 22. Comparison between experimental and numerical results for the thickness distributions at the end of forming process in RD for *vonMises*, *Hill*48 – *evp* and *Barlat*91 criteria without kinematic hardening.

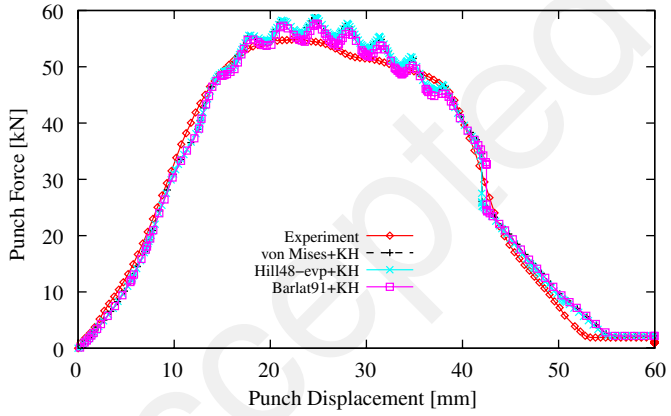

Fig. 21. Comparison between experimental and numerical results for the evolution of force during forming process for *vonMises* + *KH*, *Hill*48 − *evp* + *KH* and *Barlat*91 + *KH* criteria with kinematic hardening.

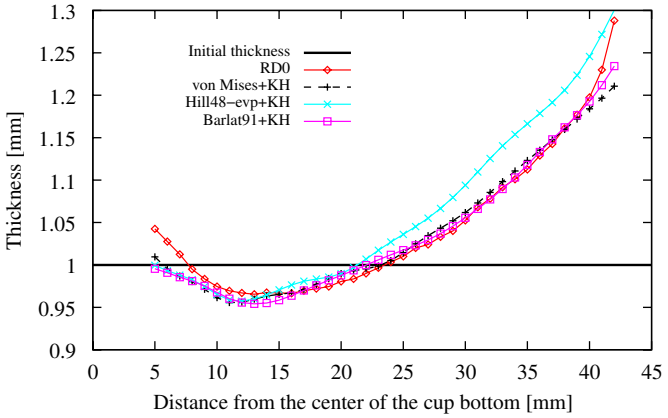

Fig. 23. Comparison between experimental and numerical results for the thickness distributions at the end of forming process in RD for *vonMises* + *KH*, *Hill*48 − *evp* + *KH* and *Barlat*91 + *KH* criteria with kinematic hardening.

region to be removed is exerting on the remaining part of the model at the nodes on their boundary. These forces are decreased to zero during the removal step; therefore, the effect of the removed region on the rest of the model is completely absent during the end of the computation. The forces are ramped down gradually to ensure that element removal has a smooth effect on the model. No further element calculations are performed for elements being removed, starting from the beginning of the step in which they are removed. The ring is finally split by removing a boundary condition of symmetry at one end of the ring and then springback is calculated by letting the part relax (Fig. 19).

6.1. *Influence of plastic yield criteria on the deep drawing simulation*

Figs. 20–27 compare the experimental results with the numerical simulations with several yield criteria. Numerical predictions are close to the experimental curves regarding the drawing process prediction. The punch force–displacement curves show that experimental and numerical results are in good agreement for all material models (Figs. 20 and 21). But for all anisotropy criteria, taking into account of a kinematic contribution improves the prediction of force evolution during the process: the maximum punch force is slightly higher with kinematic hardening but, after a punch displacement of 30 mm,

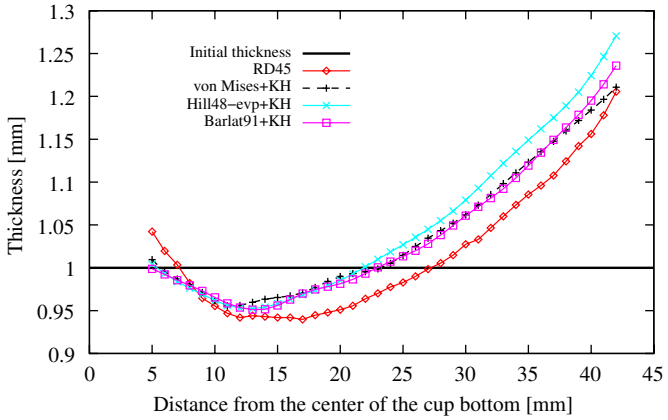

Fig. 24. Comparison between experimental and numerical results for the thickness distributions at the end of forming process at 45° to RD for *vonMises* + *KH*, *Hill*48 − *evp* + *KH* and *Barlat*91 + *KH* criteria with kinematic hardening.

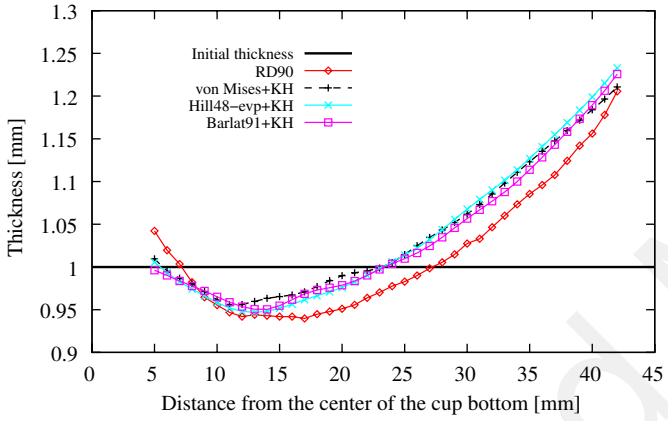

Fig. 25. Comparison between experimental and numerical results for the thickness distributions at the end of forming process at 90° to RD for *vonMises* + *KH*, *Hill*48 − *evp* + *KH* and *Barlat*91 + *KH* criteria with kinematic hardening.

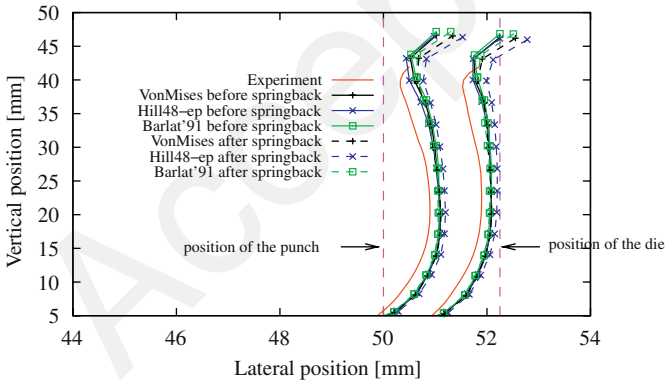

Fig. 26. Comparison between experimental and numerical results of the wall profile, for the inner and outer surfaces, at the end of forming process for *vonMises*, *Hill*48 − *evp* and *Barlat*91 criteria without kinematic hardening.

the punch force evolution is better described with this hardening law. Moreover, the numerical friction coefficient seems to be correctly chosen considering the final force stagnation at around 2 kN; this stagnation is related to the friction of the top of the cup on the drawing die. A significant force oscillation can also be

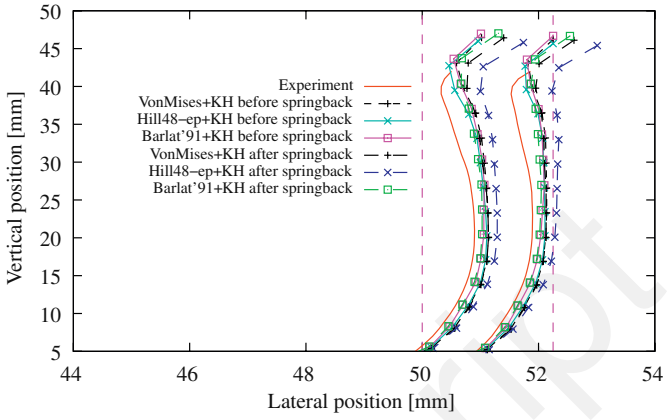

Fig. 27. Comparison between experimental and numerical results of the wall profile, for the inner and outer surfaces, at the end of forming process for *vonMises*, *Hill*48 − *evp* and *Barlat*91 criteria with kinematic hardening.

Table 6
Ring height (in mm) before springback with different yield criteria with or without kinematic hardening.

Yield criterion	Isotropic hardening			Isotropic hardening + KH		
	0°	45°	90°	0°	45°	90°
vonMises	19.42	19.42	19.42	19.37	19.37	19.37
*Hill*48 − *evp*	19.32	19.22	19.24	19.15	19.25	19.19
*Barlat*91	19.66	19.48	19.41	19.6	19.4	19.26

noticed, which is justified by the flow into the die radius zone of high in-plane size finite elements.

The thickness distributions in RD are shown in Figs. 22 and 23 with or without kinematic hardening, respectively. Predicted thickness distribution using the *Hill*48 − *evp* yield criterion is slightly higher than experimental thickness distribution and than those obtained with the two other yield criteria. Taking into account of kinematic hardening (Fig. 23) slightly improves the quality of the thickness evolution only for *Barlat*91 criterion. Simulations using the *von Mises* model show relatively good results for the thickness distribution along the RD, whereas numerical results are not that accurate in the other orientations (Figs. 24 and 25).

It is important to notice that, before springback, the cutting operation performed with the element removal option in Abaqus will not guarantee that all rings will have exactly the same height. Table 6 presents the ring height obtained for all the models and the discrepancy to the theoretical value of 20 mm. These results are in agreement with the thickness distributions presented in Figs. 22 and 23 which show a lower stretching with *Hill48-evp* criterion. Anyway, ring height presents a maximum deviation of 5% with this yield criterion.

Figs. 26 and 27 present the comparison between the experimental wall profile and the predicted one with all yield criteria, with and without kinematic hardening, respectively. In these figures, the springback obtained after the removal of the drawing tools and the positions of the punch and die are shown. There is a large gap between the punch and the die, thus the top of the wall has a higher springback. All the criteria give close results but the numerical wall profile seems to be more vertical. This difference between numerical and experimental results is mainly induced during forming stage.

Table 7
Springback values (in mm) calculated with different yield criteria with or without kinematic hardening with C3D8I elements.

Experimental 64		
Yield criterion	Isotropic hardening	Isotropic hardening + KH
vonMises	55	48
*Hill*48 – *evp*	36	29
*Barlat*91	64	61

6.2. *Influence of plastic yield criteria on the springback prediction*

Table 7 presents experimental and numerical results for the ring openings. Springback predictions are relatively different from experimental values which confirms that springback predictions in aluminum alloys hardly present good results e.g. [1,20,45]. However, simulation results show that material models and plastic yield criteria have a large influence on springback estimation. Generally speaking, using isotropic and kinematic hardening simultaneously tends to decrease the springback estimation whereas isotropic hardening leads to higher values. Considering the yield functions, *Barlat*91 gives the best prediction for ring opening while the others are quite far from experimental data. It is interesting to note that simulations using the *Hill*48 – *evp* yield function give the worst results. The low *r*-value of the anisotropy coefficients of the AA5754 can explain this bad result with this yield criterion. This finding, which is similar to those previously obtained by other authors [5,46], shows that the Hill transverse anisotropic formulation, while suitable for steels, is questionable in its applicability towards low *r* material such as aluminum.

6.3. *Discussion*

Residual stresses in the cup exist due to a gradient of circumferential stresses. These stresses have a key role in the modeling of springback because their integral over the thickness yields a non-zero bending moment and thus a shape change. Therefore, to further investigate the origin of the springback, stress distribution through the thickness before cutting and after springback is analyzed. The radial, tangential and axial stresses in the cylindrical frame defined in Fig. 16(b) are examined.

A local coordinate system has been defined in the numerical model. The variation of stresses between the inner and outer skins of the blank along the cup circumference is shown in Fig. 28, before trimming and after springback, for the *von Mises* yield criterion without kinematic hardening. Observed nodes are in the mid-height of the cut ring and depend on the angle to RD. It is observed that the cylindrical cup presents residual stresses only in the tangential and axial directions. Tangential and axial stress gradients between inner and outer skins are significant whereas the radial stress one is close to zero. It is shown that radial stresses are not affected by cutting and splitting operations whereas tangential and axial stresses are. Trimming and splitting the ring release the residual stresses that modify the shape of the part. The non-symmetrical distribution of tangential stresses between the wall surfaces induces springback and the opening of the ring. Concerning the axial stresses, the same phenomenon appears and induces a conical shape of the ring after splitting.

Figs. 29 and 30 focus on the tangential stress variation through the thickness of the cup for all criteria, in the mid-height of the cut ring before springback. Results are presented at 90° to RD. Thickness 0 corresponds to the interior part of the cup and thickness 1 to the exterior part. It is observed that the inner skin is in a compressive stress state, whereas the outer skin is in tension. At the end of the drawing operations, the neutral fiber is clearly located in the tensile stress area. This characteristic stress state before unloading leads to a large bending moment, hence a large amount of springback in this region.

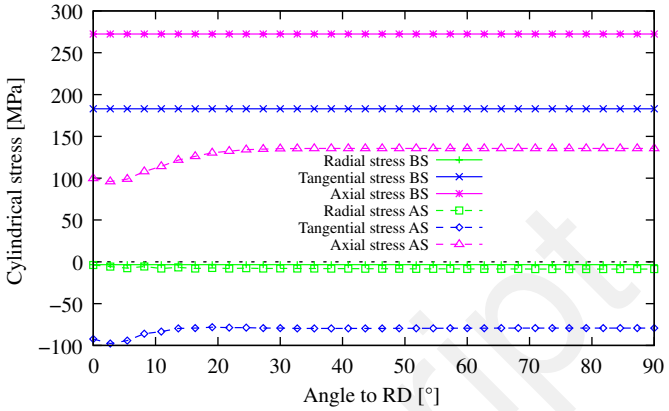

Fig. 28. Variation of radial ($\Delta\sigma_{rr}$), tangential ($\Delta\sigma_{\theta\theta}$) and axial stresses ($\Delta\sigma_{zz}$) along the cup circumference for *von Mises* criterion without kinematic hardening (BS denotes before springback and AS, after springback).

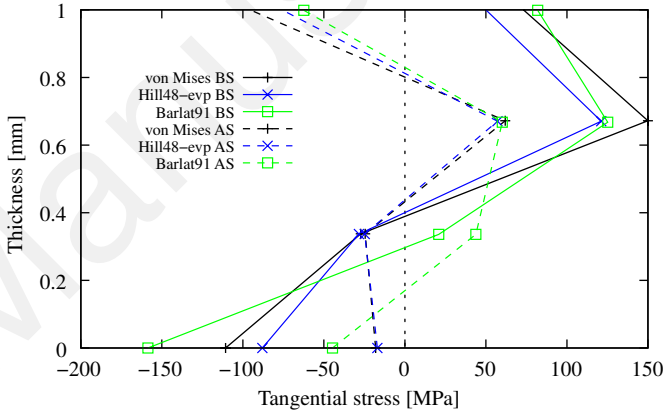

Fig. 29. Tangential stress distribution through the thickness in the mid-height of the cut ring for *vonMises*, *Hill*48 – *evp* and *Barlat*91 criteria without kinematic hardening.

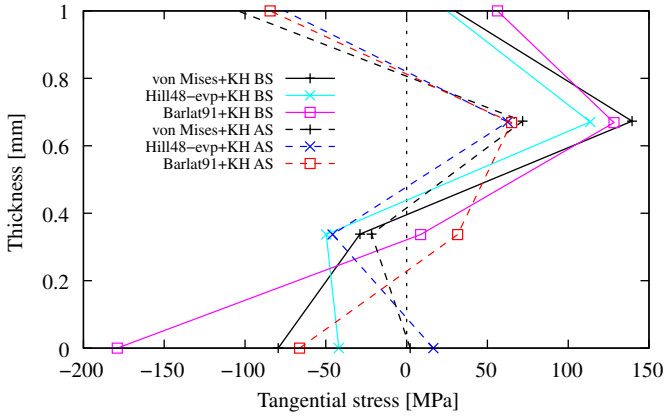

Fig. 30. Tangential stress distribution through the thickness in the mid-height of the cut ring for *vonMises*, *Hill*48 – *evp* and *Barlat*91 criteria with kinematic hardening.

Fig. 31 shows the difference between the tangential stresses before and after springback presented in Figs. 29 and 30. There is a through-thickness gradient of the tangential stress variation, before and after springback. The tangential stress state after springback is not symmetric to the mid-plane of the sheet. This asymmetry of the stress state is probably due to the friction along the die radius which induces a shearing of the blank. Anymore, classically, the gradient of the tangential stress before and after cutting follows a quasi-linear evolution through the thickness of the part.

The variation of the tangential stress gradient between inner and outer skins as a function of the height in the cup wall is plotted in Figs. 32 and 33. This evolution follows a straight line located at 90° to RD. It is interesting to note that the bottom part of the cup is in a global compressive stress state, which is in good agreement with the fact that rings cut in this area close over themselves. The top part of the cup is on the contrary, in tension, which is also coherent with Xia's experiments on the split-ring test [18]. The variation of the tangential stress state along the cup height is directly linked to the variation of the opening of the ring according to its cutting height. The tangential stress state appears to be the main factor that influences springback.

Figs. 32 and 33 show also a slightly different distribution of the gradient of the tangential stress when taking kinematic hardening into account, in particular with *Barlat*91 criterion, which can explain the small gap in the prediction of springback. Nevertheless, in this case, the change in the opening is located within the experimental scatter.

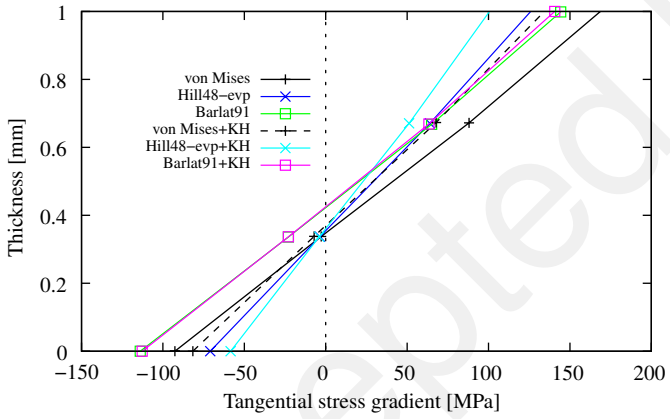

Fig. 31. Gradient of the tangential stress before and after springback.

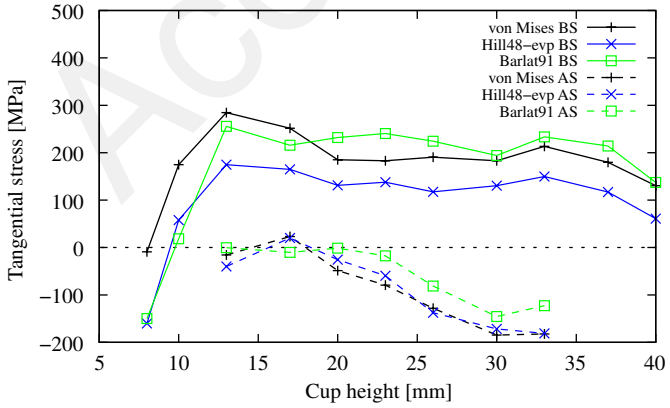

Fig. 32. Gradient of the tangential stress between inner and outer skins vs height in the cup wall for *vonMises*, *Hill*48 – *evp* and *Barlat*91 criteria without kinematic hardening.

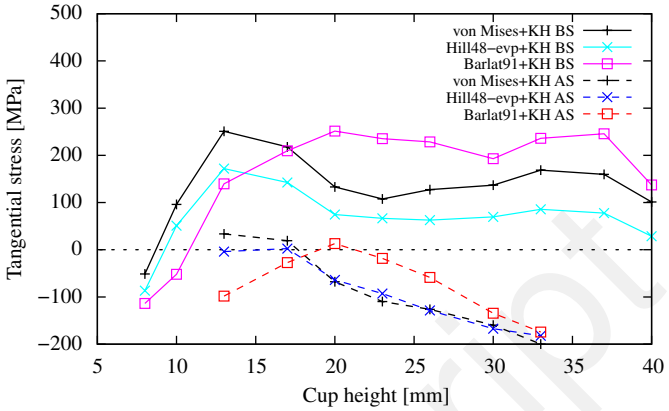

Fig. 33. Gradient of the tangential stress between inner and outer skins vs height in the cup wall for *vonMises*, *Hill*48 – *evp* and *Barlat*91 criteria with kinematic hardening.

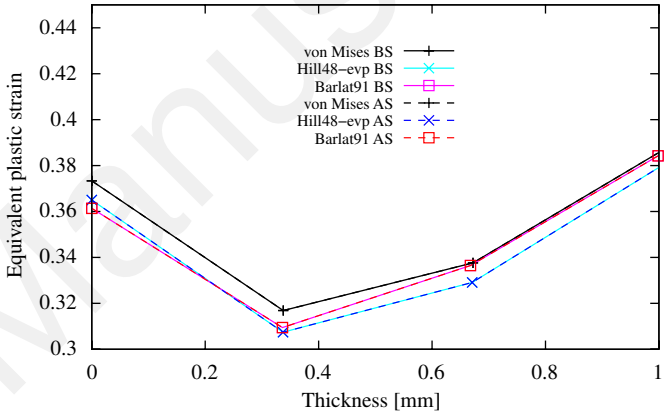

Fig. 34. Equivalent plastic strain distribution through the thickness in the mid-height of the cut ring for *vonMises*, *Hill*48 – *evp* and *Barlat*91 criteria without kinematic hardening.

The last parameter examined is the evolution of the equivalent plastic strain through the thickness of the cup. Fig. 34 presents the values calculated before and after splitting for yield criteria without kinematic hardening. This figure shows that the cutting operations induce only elastic phenomena as the plastic strain curves before and after splitting are perfectly superposed.

7. Conclusions

In this paper, a detailed experimental and numerical study of springback using the split-ring test for AA5754-O is proposed. The whole experimental and numerical process, using the software Abaqus of the split-ring test is described. Numerical results provide good correlation with experimental data during the forming analysis which demonstrates that simulations are able to predict certain aspects of the forming process fairly well, such as evolution of force during forming, thickness distributions and deformation profile. Numerical results, in this case, also show that the constitutive model has a minor influence on drawing operations. On the other hand, the springback can hardly be accurately estimated: the results indicate a higher impact of the yield criteria than the hardening law. The predicted opening using von Mises and Hill'48 criteria with kinematic hardening was less accurate than those obtained using the Barlat'91 model. A detailed study of the stress distribution in the thickness of the blank shows that the yield criteria and hardening models are critical in

determining the distribution of the stress in the cup. The numerical prediction of the tangential stress in the cup wall seems to explain some observations of the springback mechanism, but it seems rather difficult to predict the complex strain path during the forming stage which induces residual stresses.

Acknowledgments

This research was supported by the "Région Bretagne" (France), the European Union and by a Marie Curie Intra-European Fellowship within the 7th European Community Framework Programme (PIEF-GA-2008-220688).

References

[1] Demeri MY, Lou M, Saran MJ. A benchmark test for springback simulation in sheet metal forming. In: Society of Automotive Engineers, Inc., vol. 01-2657, 2000.
[2] Geng L, Wagoner RH. Role of plastic anisotropy and its evolution on springback. International Journal of Mechanical Sciences 2002;44:123–48.
[3] Oliveira MC, Alves JL, Chaparro BM, Menezes LF. Study on the influence of work-hardening modeling in springback prediction. International Journal of Plasticity 2007;23(3):516–43.
[4] Banabic D. Formability of metallic materials. Berlin, Heidelberg: Springer; 2000.
[5] Harpell ET, Worswick MJ, Finn M, Jain M, Martin P. Numerical prediction of the limiting draw ratio for aluminum alloy sheet. Journal of Materials Processing Technology 2000;100(1–3):131–41.
[6] Thuillier S, Manach PY, Menezes LF, Oliveira MC. Experimental and numerical study of reverse re-drawing of anisotropic sheet metals. Journal of Materials Processing Technology 2002;125–126:764–71.
[7] Wu HC. Anisotropic plasticity for sheet metals using the concept of combined isotropic-kinematic hardening. International Journal of Plasticity 2002;18: 1661–82.
[8] Gallée S, Manach PY, Thuillier S. Mechanical behavior of metastable austenitic stainless steel under simple and complex loading paths. Material Science and Engineering A 2007;466:47–55.
[9] Barlat F, Maeda Y, Chung K, Yanagawa M, Brem JC, Hayashida Y, et al. Yield function development for aluminum alloy sheets. Journal of the Mechanics and Physics of Solids 1997;45(11–12):1727–63.
[10] Barlat F, Lege DJ, Brem JC. A six-component yield function for anisotropic materials. International Journal of Plasticity 1991;7:693–712.
[11] Barlat F, Brem JC, Yoon JW, Chung K, Dick RE, Lege DJ, et al. Plane stress yield function for aluminum alloy sheets—part I: theory. International Journal of Plasticity 2003;19:1297–319.
[12] Karafillis AP, Boyce MC. A general anisotropic yield criterion using bounds and a transformation weighting tensor. Journal of the Mechanics and Physics of Solids 1993;41:1859–86.
[13] Bron F, Besson J. A yield function for anisotropic materials application to aluminum alloys. International Journal of Plasticity 2004;20(4–5):937–63.
[14] Xia ZC, Miller CE, Ren F. Springback behavior of AA6111-T4 with split-ring test. In: Ghosh S, Castro JC, Lee J, editors, Numiform, 2004. p. 934–9.
[15] Echempati R, SathyaDev VMS. Spring back studies in aluminium alloys. In: Society of Automotive Engineers, Inc., vol. 01-1057, 2002.
[16] Hsu CW, Ulsoy AG, Demeri MY. Development of process control in sheet metal forming. Journal of Materials Processing Technology 2002;127(3):361–8.
[17] Foecke T, Gnaeupel-Herold T. Robustness of the sheet metal springback cup test. Metallurgical and Material Transactions A 2006;37A:3503–10.
[18] Xia ZC, Miller CE, Ren F. Experimental and numerical investigations of a split-ring test for springback. Journal of Manufacturing Science and Engineering 2007;129:352–9.
[19] Grèze R, Laurent H, Manach PY. Springback study in aluminum alloys based on the Demeri benchmark test: influence of material model. In: Cueto E, Chinesta F, editors, 10th Esaform conference on material forming, vol. 907, AIP conference proceedings, Zaragoza, Spain, 2007. p. 1512–7.
[20] Baptista AJ, Oliveira MC, Rodrigues DM, Menezes LF. Springback evaluation applying the splitting ring benchmark test in tailor welded blanks. In: IDDRG International Deep Drawing Research Group, 2004. p. 307–17.
[21] Abaqus, Hibbit, Karlson and Sorensen Inc., Theory Manual—version 6.5 edition, 2005.
[22] Xiao H, Bruhns OT, Meyers A. On objective corotational rates and their defining spin tensors. International Journal of Solids and Structures 1998; 35(30):4001–14.
[23] Simo J, Hughes T. Computational inelasticity. Berlin, Heidelberg: Springer; 1998.
[24] Ponthot J-P. Unified stress update algorithms for the numerical simulation of large deformation elasto-plastic and elasto-viscoplastic processes. International Journal of Plasticity 2002;18:91–126.
[25] Rio G, Laurent H, Blès G. Asynchronous interface between a finite element commercial software ABAQUS and an academic research code HEREZH + +. Advances in Engineering Software 2008;39(12):1010–22.
[26] Hill R. A theory of the yielding and plastic flow of anisotropic metals. Proceedings of the Royal Society of London Series A 1948;193: 281–97.
[27] Hershey AV. The plasticity of an isotropic aggregate of anisotropic face centered cubic crystals. Journal of Applied Mechanical Transactions ASME 1954;21:241.
[28] Hosford WF. A generalized isotropic yield criterion. Journal of Applied Mechanical Transactions ASME E 1972;39:607.
[29] Chung K, Shah K. Finite element simulation of sheet metal forming for planar anisotropic metals. International Journal of Plasticity 1992;8: 453–76.
[30] Armstrong PJ, Frederick CO. A mathematical representation of the multiaxial Bauschinger effect. Technical Report, CEGB Berkeley Nuclear Laboratories; 1966.
[31] Thuillier S, Manach PY. Comparison of the work-hardening of metallic sheets using tensile and shear strain paths. International Journal of Plasticity 2008, in press, doi:10.1016/j.ijplas.2008.07.002.
[32] Picu RC, Vincze G, Ozturk F, Gracio JJ, Barlat F, Maniatty AM. Strain rate sensitivity of the commercial aluminum alloy AA5182. Materials Science and Engineering A 2005;390:334–43.
[33] Manach PY, Couty N. Elastoviscohysteresis constitutive law in convected coordinate frames: application to finite deformation shear tests. Computational Mechanics 2001;28:17.
[34] Rauch EF, G'Sell C. Flow localisation induced by a change in strain path in mild steel. Materials Science and Engineering A 1989;111:71–80.
[35] Cailletaud G, Pilvin P. Identification and inverse problems related to material behaviour. In: International seminar on inverse problems, Clamart, France, 1994. p. 79–86.
[36] Andrade-Campos A, Thuillier S, Pilvin P, Teixeira-Dias F. On the determination of material parameters for internal variable thermoelastic–viscoplastic constitutive models. International Journal of Plasticity 2007;23(8):1349–79.
[37] Chaparro BM, Thuillier S, Menezes LF, Manach PY, Fernandes JV. Material parameters identification, genetic and hybrid optimization algorithms: gradient-based. Computational Materials Science 2008;44(2):339–46.
[38] Haddag B, Balan T, Abed-Meraim F. Investigation of advanced strain-path dependent material models for sheet metal forming simulations. International Journal of Plasticity 2007;23(6):951–79.
[39] Iadicola MA, Foecke T, Banovic SW. Experimental observations of evolving yield loci in biaxially strained AA5754-O. International Journal of Plasticity 2008;24(11):2084–101.
[40] Kim JH, Lee M-G, Barlat F, Wagoner RH, Chung K. An elasto-plastic constitutive model with plastic strain rate potentials for anisotropic cubic metals. International Journal of Plasticity 2008;24(12):2298–334.
[41] Grytten F, Holmedal B, Hopperstadand OS, Borvik T. Evaluation of identification methods for YLD2004-18p. International Journal of Plasticity 2008; 24(12):2248–77.
[42] Simo JC, Armero F. Geometrically nonlinear enhanced strain mixed methods and the method of incompatible modes. International Journal for Numerical Methods in Engineering 1992;33:1413–49.
[43] Adam L, Ponthot J-P. Thermomechanical modeling of metals at finite strains: first and mixed order finite elements. International Journal of Solids and Structures 2005;18(1):5615–55.
[44] Parente MPL, Valente RAF, Jorge RMN, Cardoso RPR, de Sousa RJA. Sheet metal forming simulation using EAS solid-shell finite elements. Finite Elements in Analysis and Design 2006;42(13):1137–49.
[45] Li X, Yang Y, Wang YI, Bao J, Li S. Effect of the material-hardening mode on the springback simulation accuracy of V-free bending. Journal of Materials Processing Technology 2002;123(2):209–11.
[46] Barlat F, Lian JL. Plastic behavior and stretchability of sheet metals. Part I: a yield function for orthotropic sheets under plane stress conditions. International Journal of Plasticity 1989;5(1):51–66.